

1 **Experimental investigation of Apollo 16 “Rusty Rock” alteration by a lunar**
2 **fumarolic gas**

3 C. J. Renggli¹, S. Klemme¹

4 ¹ Institut für Mineralogie, Universität Münster, Münster, 48149, Deutschland

5 Corresponding author: Christian Renggli (renggli@uni-muenster.de)

6 ORCID: Renggli 0000-0001-8913-4176

7 ORCID: Klemme 0000-0001-7859-9779

8

9 **Key points**

- 10
- Experiments constrain the temperature of fumarolic Apollo 16 “Rusty Rock”
11 alteration to 580 ± 50 °C.
 - Gas deposition and gas-solid metal reaction experiments reproduce the „Rusty Rock”
12 alteration phases FeCl_2 and $(\text{Zn,Fe})\text{S}$
13

14 **Abstract**

15 The Apollo 16 sample 66095, named „Rusty Rock”, is enriched in volatile and moderately
16 volatile elements. The impact melt breccia is characterized by the abundant occurrence of Fe-rich
17 sulfide and chloride alteration phases, including FeS, ZnS and FeCl₂. These phases have previously
18 been interpreted to be the result of fumarolic alteration of the breccia. Here we present the results of
19 two different experimental approaches, which aim to constrain the temperature conditions and the
20 process under which the „Rusty Rock” alteration formed. The first experimental set-up assumes that
21 the metals Zn, Cu and Fe were introduced into the rock by a C-O-S-Cl gas phase, and that the Fe-rich
22 sulfides and chlorides were deposited from this gas phase. This “gas deposition” experiment suggests
23 that the alteration assemblage formed over the temperature range of 538-638±5 °C. The second
24 experimental set-up simulates a scenario, where Fe metal particles in the lunar rock react with a Zn-C-
25 O-S-Cl gas phase at six different temperatures between 396±5 °C and 1005±5 °C. This latter “metal
26 reaction” experiment resulted in the formation of sulfide and chloride coatings on the Fe metal chips.
27 The „Rusty Rock” alteration phases FeCl₂ and (Zn,Fe)S were abundantly present in the coating of the
28 Fe metal chip reacted at 580±5 °C. Both experiments lead to results which are in agreement,
29 providing a temperature of 580 ± 50 °C for the fumarolic alteration on the Moon, as observed in the
30 Apollo 16 „Rusty Rock”.

31 **Plain Language Summary**

32 The Apollo 16 sample 66095, colloquially named „Rusty Rock”, is an unusual lunar rock
33 which is enriched in volatile elements such as sulfur and chlorine. We investigate two processes by
34 which sulfides and chlorides may form in a lunar fumarolic system, by conducting experiments in
35 evacuated silica glass tubes at reducing conditions. First, we assume that metals and volatiles (Zn, Cu,
36 Fe, S and Cl) are all deposited from a gas phase (gas deposition experiments), and second, we assume
37 that Fe metal is already present in the rock and that the Fe altered by the introduction of a Zn-S-Cl-
38 bearing gas phase (metal reaction experiment). In both experimental setups we observe the formation
39 of „Rusty Rock” alteration phases FeCl₂ and (Zn,Fe)S at 580 ± 50 °C, constraining the temperature of

40 fumarolic alteration recorded in the Apollo 16 sample 66095. Hence, our experiments confirm that the
41 characteristic S- and Cl-rich minerals found in the lunar “Rusty Rock” were formed by a lunar
42 fumarole. More broadly, lunar metal deposits may be associated with ancient fumarolic processes.

43 **1. Introduction**

44 The Apollo 16 „Rusty Rock” 66095 is a unique lunar sample which is highly enriched in the
45 volatile elements S and Cl and in moderately volatile trace metals such as Tl, Br, Cd, Sn, Zn, Pb, Rb,
46 Cs, Ga, B and Li (Krähenbühl et al., 1973; Taylor et al., 1973; Shearer et al., 2014; Day et al., 2017;
47 Day et al., 2019). This volatile element enrichment of the „Rusty Rock” is in contrast to the vast
48 majority of lunar samples which are generally very volatile depleted relative to terrestrial magmatic
49 rocks (e.g. McCubbin et al., 2015).

50 Sample 66095 is a fine-grained impact melt breccia with lithic clasts, including anorthosite,
51 troctolite, basalt and a minor KREEP-like component. The lithic clasts further contain metallic iron-
52 nickel grains. These grains are commonly altered on the rims to $(\text{Fe,Ni})\text{Cl}_2$, $\text{FeO}(\text{OH,Cl})$, FeS and
53 occasional ZnS (Taylor et al., 1973; El Goresy et al., 1973; Taylor et al., 1974; Hunter and Taylor,
54 1981a; Hunter and Taylor, 1981b; Shearer et al., 2014). The alteration occurs on the surface of the
55 rocks as well as the interior, suggesting that it was not a secondary process that occurred after
56 sampling, in the spacecraft or on Earth (Meyer, 2009). Similar alteration features were observed in
57 more than 20 different Apollo 16 samples (Taylor et al., 1973; Jean et al., 2016). This suggests that
58 the alteration is a regional lunar process, rather than limited to sample 66095. Sulfidation (sulfide
59 formation via gas-solid reactions) is not only associated with FeNi grains, but it also occurs
60 disseminated in veins and replacement textures of olivine and pyroxene in Apollo 16 rocks (Norman,
61 1981; Colson, 1992; Norman et al., 1995; Shearer et al., 2012). This underlines the broader
62 importance of the „Rusty Rock”, which provides a unique insight into the transport of volatile
63 elements in the lunar crust.

64 Recent work has highlighted unique isotopic signatures of the Apollo 16 „Rusty Rock”
65 66095, providing insights into the origin of enriched volatile elements (Shearer et al., 2014; Day et al.,

2017; Day et al., 2019). The „Rusty Rock” is one of the most S-rich Apollo 16 samples, and with $\delta^{34}\text{S}=+1.9\%$ one of the most isotopically light lunar samples (Kerridge et al., 1975). Other lunar samples with light $\delta^{34}\text{S}$ compositions include volatile coatings on Apollo 17 pyroclastic glass beads and troilite replacement veins in Apollo 16 breccias (Shearer et al., 2012). Because the light S isotopes preferentially partition into a gas phase, isotopically light $\delta^{34}\text{S}$ in 66095 sulfides indicate that they deposited from a volcanic or fumarolic gas (Shearer et al., 2012; Shearer et al., 2014). The Cl isotopic composition of 66095, on the other hand, is heavy with respect to lunar igneous rocks, with $\delta^{37}\text{Cl}$ ranging from +14.0‰ to +15.6‰ (Sharp et al., 2010; Shearer et al., 2014; Gargano et al., 2020). Apart from lunar apatites (Wang et al., 2012; Ustunisik et al., 2015), these are the heaviest Cl isotopic compositions measured in lunar samples (Shearer et al., 2014). As the overall Cl isotopic composition of the Moon was inferred to be similar to that of the Earth, the occurrence of much heavier isotopic compositions was attributed to the volatilization of metal halides (Sharp et al., 2010; Shearer et al., 2014; Gargano et al., 2020). These metal halides were deposited from the gas phase on pyroclastic glass beads, and in altered regolith and breccia such as 66095 (Shearer et al., 2014). The isotopic composition of Zn supports the interpretation of S and Cl isotopic compositions and the $\delta^{66}\text{Zn}$ composition of the „Rusty Rock” reveals the lightest isotopic signature of Zn recorded in any sample analyzed, with $\delta^{66}\text{Zn} = -13.7\%$ (Day et al., 2017). This light isotopic signature was interpreted to be caused by degassing from a volatile-depleted Moon and condensation in the lunar regolith and on the Moon’s surface (Day et al., 2017; Day et al., 2019). Note that Cu and Fe isotopic compositions of 66095 are not fractionated and are within the range of normal lunar mare basalts ($\delta^{65}\text{Cu} = 0.9\%$, $\delta^{56}\text{Fe} = 0.1\%$) (Day et al., 2019). Iron is considered a non-volatile element but Cu is moderately volatile (Lodders, 2003; Norris and Wood, 2017; Sossi and Fegley, 2018; Sossi et al., 2019) so that stable Cu isotopes should have been fractionated if Cu had been deposited from a gas phase in the „Rusty Rock”. In a lunar volcanic gas at 1 bar and 1200 °C Zn is two orders of magnitude more volatile than Cu, and four orders of magnitude more volatile than Fe (Renggli et al., 2017).

Two different mechanisms are conceivable for the formation of the observed sulfide and chloride alteration in the „Rusty Rock” samples. In the first scenario, all metals (i.e., Zn, Cu and Fe),

93 together with S and Cl, were introduced into the rock by a fumarolic gas phase, and this caused
94 deposition of metal sulfides and chlorides (gas deposition process). For example, in such a process
95 lawrencite could be introduced into the „Rusty Rock” as a gas according to the reaction
96 $\text{FeCl}_{2(g)} = \text{FeCl}_{2(s)}$ (Colson, 1992). Similarly, Zn and Cu could be introduced as chloride, sulfide or
97 elemental gas species and deposited under the same conditions as FeCl_2 . This process would be
98 recorded in the „Rusty Rock” by light isotopic signatures of the metals and the isotopically light Zn
99 isotopes support this process (Day et al., 2017). However, the Cu and Fe isotopes are not isotopically
100 light (Day et al., 2019) and hence this process does not account for the Cu and Fe isotopic signatures
101 of 66095. In a second scenario, the metals Fe and Cu were not introduced by the gas phase, but
102 instead, they were present in the rock prior to gas metasomatism, and hence the metals Cu and Fe
103 reacted with a gas phase to form sulfides and chlorides (metal reaction process). Based on the isotopic
104 composition, the latter mechanism was proposed to explain the alteration of Cu and Fe in the „Rusty
105 Rock” (Day et al., 2019).

106 In both mechanisms a S- and Cl-bearing gas phase causes the alteration, either by introducing
107 the metals, or by reacting with the metals in the rock to cause the sulfidation and chlorination. The
108 gas-solid reactions may have occurred in ejecta blankets (Haskin and Warren, 1991) with volatiles
109 sourced from comets or meteorites, or mobilized from the crust (El Goresy et al., 1973; Papike et al.,
110 1991). Norman et al. (1995) first proposed that the source of sulfidation in Apollo 16 ferroan noritic
111 anorthosites was driven by anhydrous C-O-S-Cl vapors, derived from shallow magmatic sources in
112 the lunar crust. The role of a S-rich and H-poor gas phase was supported by Shearer et al. (2012).
113 Similarly, Shearer et al. (2014) suggested that FeCl_2 , FeS and ZnS in the „Rusty Rock” formed by a
114 H-poor C-O-S-Cl gas, without a major extra-lunar contribution. Consequently, we conduct our
115 experiments in a H-free system.

116 Our aim is to investigate these gas deposition and metal reaction processes proposed for the
117 „Rusty Rock” alteration experimentally, and constrain the temperature conditions under which the
118 „Rusty Rock” alteration (FeCl_2 , FeS , ZnS) formed. Furthermore, we aim to put constraints on the
119 fumarolic gas composition and test if the two mechanisms discussed above (deposition of Fe from the

120 gas phase vs. in-situ reaction with a C-O-S-Cl gas) are viable. For this purpose we used two different
121 experimental approaches, simulating the different proposed alteration mechanisms, where the first
122 approach assumes that all major elements of the alteration assemblage (i.e., Zn, Fe, Cu, Cl and S)
123 were transported by a gas phase to form deposits along a temperature gradient (gas deposition
124 experiment), essentially identical to the formation of mineral deposits from fumarolic gases (Renggli
125 and Klemme, 2020). The second approach assumes that the Fe metal was already present in the rock
126 and reacted with a C-O-S-Cl gas phase (metal reaction experiment). In this experiment we also
127 include Zn in the gas phase due to the evidence from light $\delta^{66}\text{Zn}$ in the „Rusty Rock”, suggesting
128 deposition from a gas phase (Day et al., 2017).

129 **2. Methods**

130 **2.1 Experimental Rationale**

131 We conducted two different gas-solid reaction experiments in evacuated silica glass tubes
132 (Fig. 1). We adopted the experimental setup from Renggli & Klemme (2020), where we showed that
133 these types of experiments can reproduce sulfide and chloride deposits in observed in terrestrial
134 fumaroles. The experimental set-up follows, in principle, Nekvasil et al. (2019), where a volatile
135 element-rich source material is placed in an evacuated silica glass tube in the hot zone of a furnace.
136 The volatile and moderately volatile elements are mobilized and transported in the gas phase, and
137 minerals are deposited in colder parts along the furnace temperature gradient. The ~30 cm long silica
138 glass tube (Fig. 1) is placed in a vertical furnace so that the starting material is in the hot zone of the
139 furnace. The furnace has a strong temperature gradient from the hot zone to the top of the furnace
140 (Fig. 1) and hence temperatures within the long glass tubes range from 1240 °C, to 316 °C at the top
141 of the glass tube (Supplement 1; Renggli and Klemme, 2020). Overall, the experimental set-up, which
142 is used to simulate the transport of metals in fumarolic gases on the Moon, is similar to natural
143 fumaroles, characterized by large gradients in temperature and variations in redox conditions, and gas
144 composition with time.

145 Our set-up does not allow precise control of the redox conditions in our experiments, as in
146 conventional gas-mixing furnaces. However, our experimental results allow us to constrain the
147 dynamic evolution of the gas phase and the redox conditions during the runs. As our starting material
148 is placed in a graphite cup, the system in the hot zone (at 1240 °C) is graphite saturated so that f_{O_2}
149 cannot exceed the C-CO buffer ($\log f_{\text{O}_2} = -16.9$ at 1240 °C and 1 bar). This buffer assemblage is only
150 operational if oxygen is present. In colder parts of the experimental glass tubes the system remains
151 reducing. Our results below show that metallic phases (e.g. Cu-whisker or Fe-metal chips) and no
152 metal oxides are present, which constrains the redox conditions at lower temperatures to below the
153 iron-wüstite buffer (see 4.1 Constraints on the gas phase composition).

154 All experiments were conducted using evacuated and sealed silica glass tubes at an initial
155 internal pressure of 10^{-5} bar. The silica glass tubes were suspended in a vertical tube furnace (Gero
156 GmbH, Germany), so that the starting material was placed in the hot zone of the furnace, i.e. 1240 °C.
157 The furnace had a temperature gradient of 900 °C from the hot zone to the top of the silica glass tube
158 (Fig. 1, Supplement 1), measured at 1 cm steps with a type B thermocouple. The temperature gradient
159 is not linear along the tube, such that the 1 cm tube segments cover temperature ranges from 15 °C at
160 the high and low temperature ends, to 65 °C where the gradient is steep around 700 °C (see Renggli
161 and Klemme 2020 for more details). We conservatively estimate a temperature error associated with
162 the preparation of the experiments of ± 5 . All experiments were run for 24 h. The starting material
163 mixtures reacted at high temperature (1240 °C) to form a gas phase that subsequently moved upwards
164 along the temperature gradient over the duration of the run (Nekvasil et al., 2019). The amount of
165 starting materials in the pellets was limited to 0.05 g. This quantity was chosen to avoid an
166 overpressurization of the ampules ($P < 3$ bar), assuming that the entire pellet material was in the gas
167 phase at 1250 °C and give the inner volume of the sealed ampules (4 mm inner diameter, $\sim 3770 \text{ mm}^3$,
168 see Renggli and Klemme 2020). The pressure in the experiments is not constant and evolves with
169 time. Initially, as the volatile elements form a gas phase the pressure increases and rapidly equilibrates
170 throughout the ampule, and gas species move along the temperature gradient by Soret diffusion

171 (Nekvasil et al., 2019). As the solid phases begin to deposit from the gas phase on the silica glass tube
172 wall the pressure decreases again (Renggli and Klemme, 2020).

173 **2.2 Experiments**

174 Our starting material mixtures consisted of reagent grade oxides, sulfides and chlorides as the
175 volatile sources for the experiments, instead of synthetic silicate melts (Ustunisik et al., 2015;
176 Nekvasil et al., 2019), to produce larger amounts of transported metals (Renggli and Klemme, 2020).
177 The reagents were pressed into pellets (2 mm diameter) in a pellet press and at room temperature. The
178 pellets were subsequently dried at 50 °C over night and placed in graphite crucibles at the bottom of
179 the silica glass tubes.

180 The first type of experiments, which we call “gas deposition experiments”, simulates the
181 transport of Zn, Cu and Fe in a C-O-S-Cl gas and the resulting deposition of sulfide and chloride
182 phases (Renggli and Klemme, 2020). The starting material was a mixture of ZnO, FeS, CuS, MgCl₂
183 and C in the relative molar abundances of 1-1-1-3-4 (Table 1), pressed into a 50 mg pellet and placed
184 in an open graphite crucible, which was then placed at the bottom of a 30 cm long evacuated silica
185 glass tube. Upon heating, the volatile reagents in the pellet form a gas (at 1240 °C) with equal molar
186 concentrations of Zn, Fe and Cu, and equal molar concentrations of S and Cl. MgO was the only solid
187 that remained in the graphite crucible after the experiment (Supplement 2).

188 In the second type of experiments, which we call “metal reaction experiments”, we
189 investigated the reaction of Fe metal with a Zn-C-O-S-Cl gas phase at 396±5, 496±5, 580±5, 708±5,
190 825±5 and 1005±5 °C. These temperatures reflect the positions of the metal chips relative to the
191 temperature gradient in the tube furnace at 7, 11, 13, 15, and 21 cm from the top of the furnace
192 respectively (Table 2, Supplement 1), with a ±5 °C temperature uncertainty resulting from the
193 positioning of the tube in the furnace. As the source of volatiles, a pellet containing a mixture of ZnO,
194 MgCl₂, S and C in the relative molar abundances of 1-1-1-4 (Table 1) was pressed and placed in an
195 open graphite crucible in the evacuated silica glass tube. In this experiment, volatilization of the
196 starting material pellet forms a gas with relative abundances of Zn:S:Cl = 1:1:2. After the experiment
197 the remaining pellet only consisted of MgO (Supplement 2), which is evidence for complete

198 volatilization of Zn, S and Cl. Iron metal chips with diameters of ~ 1 mm were placed on silica glass
199 wool spacers along the tube prior to the evacuation of the tube. The contact of the Fe metal chips with
200 the silica glass wool resulted in the formation of minor amounts of Fe₂SiO₄.

201 .

202 The silica glass tubes were lifted out of the furnace and quenched in cold water. The
203 quenched tubes were cold within less than 10 seconds, minimizing secondary alteration within the
204 tubes. The tubes were then cut in 1cm long segments, corresponding to the position of the tubes
205 relative to the temperature gradient in the furnace (Supplement 1). The samples were immediately
206 placed in an evacuated desiccator in order to avoid alteration by exposure to the humidity in the air
207 (Dalby et al., 2018). Aliquots of the reacted Fe metal chips were embedded in epoxy resin and
208 prepared as polished cross-sections. The mounts were polished dry without water to avoid hydration
209 of the samples, however the chlorides partially hydrated during sample preparation.

210 All samples were characterized with a JSM-6610 Series Scanning Electron Microscope
211 (SEM). The silica tube segments with the sulfide and chloride deposits on the inner silica glass tube
212 wall were analyzed without carbon coating using the low-vacuum capability of the SEM at 50 Pa.
213 This allowed a minimization of sample exposure to ambient air and modification during sample
214 preparation. The cross-sectioned samples were carbon coated and analyzed and imaged at high-
215 vacuum using the Back-Scattered Electron (BSE) detector. All EDS analysis (both of the reacted
216 surfaces and the cross-sectioned samples) were done at an acceleration voltage of 20 kV and a
217 working distance of 10 mm, using the JEOL EDS analysis station with a dry silicon drift detector. The
218 JEOL software performs and automated EDS peak identification and integrates the spectra to provide
219 semi-quantitative atomic abundances. Due to the chemical simplicity of our experimental system no
220 significant peak overlap is observed in the EDS spectra, allowing the integration of the spectra and the
221 extraction of the compositions of the experimental phases. We analyzed each observed phase 5-10
222 times and provide standard deviations. We report the results of the EDS analysis as atomic% (Table 3
223 and Table 4).

224 3. Results

225 3.1 Gas deposition experiments

226 We observe eight different phases deposited on the inner wall of the silica glass tube, over the
227 entire temperature range from 330-1240 °C (Fig. 2, Table 3). With the exception of forsterite
228 (Mg_2SiO_4), which forms as the product of a reaction of the starting material with the silica glass tube,
229 the phases were deposited from the Zn-Fe-Cu-C-O-S-Cl gas. We observe forsterite only at high
230 temperatures ($T > 698 \pm 5$ °C) with grain sizes of up to 20 μm . This suggests that minor amounts of the
231 MgCl_2 in the starting material were transported in the gas phase and reacted with the hot silica glass
232 tube wall. The only chemical compound remaining in the graphite crucible after the experiment is
233 MgO , suggesting that gas phase transport of Mg was a minor process. The MgO forms a dense pellet
234 with grain sizes of up to 20 μm (Supplement 2). Phases deposited from the gas phase are spread over
235 almost the entire silica tube from 330-1140 \pm 5 °C, with little overlap of different phases (Fig. 3).

236 Chalcocite (Cu_2S) occurs between 878 \pm 5-1140 \pm 5 °C and forms tabular grains often deposited
237 in patches or groups of multiple single crystals (Fig. 2a & b). Below 1000 °C the crystals form
238 increasingly well-developed crystal faces, whereas the typical habit of chalcocite crystals is more
239 rounded at higher temperatures, especially in the case of crystals deposited near the melting point of
240 Cu_2S at 1130 °C. The crystals have diameters of up to 60 μm and are commonly associated with
241 higher abundances of forsterite on the tube wall. All chalcocite crystals show the growth of Cu-metal
242 whiskers extruding from their surface (Fig. 2b). The whiskers have lengths of up to 10 μm and are
243 composites of copper fibers with sub-micron diameters. At 698 \pm 5-830 \pm 5 °C (Fig. 3) we observe an
244 unidentified Fe-Cu-S-Cl phase. These rare crystals have diameters of \sim 40 μm and well-developed
245 triangular crystal faces.

246 The largest quantities of metal sulfide and chloride deposits occur over the relatively narrow
247 temperature range of 540 \pm 5-700 \pm 5 °C (Fig. 3). In this narrow temperature range we observe the
248 phases described in the Apollo „Rusty Rock”, including FeS, lawrencite (FeCl_2) and wurtzite (ZnS).
249 FeS (presumed troilite) (638 \pm 5-698 \pm 5 °C) forms platy crystals and occurs together with lawrencite

250 (Fig. 3d). The FeS plates have diameters of up to 200 μm . Lawrencite occurs over a wider temperature
251 range of 538 ± 5 - 698 ± 5 $^{\circ}\text{C}$ (Fig. 2). Where lawrencite coexists with FeS (Fig. 2d) the crystals are
252 small, with prismatic grains up to 10 μm in length. At slightly lower temperature ($>638\pm 5$ $^{\circ}\text{C}$) the
253 lawrencite forms large platy grains (Fig. 2e). Between 538 ± 5 and 587 ± 5 $^{\circ}\text{C}$ we observe a sharp
254 boundary between a lawrencite and wurtzite dominated section (Fig. 2f). In the wurtzite dominated
255 section we observe occasional triangular, platy FeCl_2 grains (Fig. 2g). The occurrence of wurtzite is
256 limited to a narrow temperature range of 538 ± 5 - 587 ± 5 $^{\circ}\text{C}$ (Fig. 3). The typical hexagonal shape of
257 wurtzite is only occasionally observed, but here we find that it forms dense aggregations of
258 intergrown ZnS crystals (Fig. 2g). Below 538 ± 5 $^{\circ}\text{C}$ we only observe Zn-phases and no Cu- or Fe-
259 bearing minerals. Below 498 ± 5 $^{\circ}\text{C}$ the only phase observed is ZnCl_2 (Fig. 3). ZnCl_2 is highly
260 deliquescent and rapidly absorbs enough water from the atmosphere to form an aqueous solution,
261 once exposed to air. This process occurs within less than 5 minutes in the relatively humid air of
262 Münster in the summer, apparent in all samples where ZnCl_2 is present (Fig. 2i). Finally, in the
263 transitional temperature range between 498 ± 5 and 538 ± 5 $^{\circ}\text{C}$ (Fig. 3) we observe an unidentified Zn-
264 phase containing both S and Cl (Fig. 2h).

265 **3.2 Metal reaction experiments**

266 The Fe metal chips reacted with a C-O-S-Cl-Zn gas at 396 ± 5 , 496 ± 5 , 580 ± 5 , 708 ± 5 , 825 ± 5
267 and 1005 ± 5 $^{\circ}\text{C}$, and the run products show that the reaction resulted in extensive reaction coatings
268 with variable amounts of FeCl_2 , $(\text{Zn,Fe})\text{S}$ and FeS (Table 4). In Figures 4 and 5 we show
269 backscattered electron images of the surface coatings on the metal chips and polished cross-sections
270 of the coated Fe metal chips. With increasing temperature, the coatings become thicker and coarser
271 grained (Fig. 5). This proved to be problematic during the sample polishing of the cross-sections for
272 SEM analysis, as the sulfide coatings partially decoupled from the underlying Fe metal chips.

273 At 396 ± 5 $^{\circ}\text{C}$ the coating almost exclusively contains FeCl_2 (lawrencite) which crystallized as
274 prismatic crystals with lengths of up to 200 μm and thicknesses of up to 40 μm (Fig. 4a). On the
275 surface coatings we did not observe any sulfide phase. In cross-section it's evident that the coatings

276 are thin with thicknesses of up to 20 μm (Fig. 4a & b). In addition to lawrencite we also detected
277 traces of S by EDS. However, we could not observe individual grains.

278 At 496 ± 5 $^{\circ}\text{C}$ lawrencite forms a dense and fine-grained coating on the reacted Fe metal (Fig.
279 4d). Individual grains are small with diameters of less than 5 μm . In cross-section we observe that the
280 coating is much thicker than at 396 ± 5 $^{\circ}\text{C}$, measuring up to 80 μm (Fig. 4e & f). We also observe
281 reaction between the lawrencite and the epoxy resin in which the sample is embedded (Fig. 4f). This
282 secondary alteration of the coating likely occurred during embedding in the liquid resin as it did not
283 change once the resin hardened.

284 At 580 ± 5 $^{\circ}\text{C}$ we observe FeCl_2 and $(\text{Zn,Fe})\text{S}$ in the coating of the Fe metal chip (Fig. 4g). The
285 coating is fine-grained with individual $(\text{Zn,Fe})\text{S}$ crystals with diameters of up to 8 μm . The coating
286 has partially engulfed silica glass fibers on which the Fe metal chip was placed (Fig. 4g). In cross-
287 section we observe that the coating with a thickness of up to 150 μm partially detached from the
288 metal, suggesting a poor cohesion (Fig. 4h & i). The coating appears to be layered, with the FeCl_2 on
289 the metal chip and the sulfide on the surface (Fig. 4i).

290 At 708 ± 5 $^{\circ}\text{C}$ $(\text{Zn,Fe})\text{S}$ dominates the coating and only traces of FeCl_2 are observed in cross-
291 section (Fig. 5 a-c). The sulfide grains have diameters of up to 40 μm (Fig. 5a), with a total coating
292 thickness of ~ 100 μm (Fig. 5b). Traces of FeCl_2 were detected in the coating by EDS, but individual
293 grains could not be identified unambiguously, suggesting grain sizes of less than 2 μm .

294 At 825 ± 5 $^{\circ}\text{C}$ the coating only contains sulfides. It is the only sample where pure FeS could be
295 distinguished from $(\text{Zn,Fe})\text{S}$. At the surface of the coating grains have diameters of up to 60 μm (Fig.
296 5d). The coating is dense and the individual sulfide crystals are euhedral. The coating is partially
297 detached from the underlying Fe metal chip (Fig. 5e), but in some sections the contact is observed.
298 The pure FeS is in direct contact with the metal chip and forms an undulatory interface (Fig. 5f). The
299 $(\text{Zn,Fe})\text{S}$ occurs on the surface of the coating.

300 Finally, at 1005 ± 5 $^{\circ}\text{C}$ the coating mainly consists of $(\text{Fe,Zn})\text{S}$ (Fig. 5 g-i). The sulfide grains
301 have diameters of up to 50 μm . The coating thickness exceeds 200 μm and was mostly lost during

302 preparation of the cross-sections (Fig. 5h). The surface of the reacted Fe metal chip is highly
303 undulatory and porosity is observed to a depth of 200 μm (Fig. 5h & i). The pore space formed during
304 the reaction with the C-O-S-Cl-Zn gas and suggests a mobilization of Fe at 1005 ± 5 $^{\circ}\text{C}$. Indeed, apart
305 from (Fe,Zn)S we also observe fayalite (Fe_2SiO_4) in the coating (Fig. 5g & i). The fayalite is primarily
306 located where the Fe metal chip was in contact with the silica glass wool or the wall of the silica glass
307 tube, facilitating the reaction.

308 In summary, 580 ± 5 $^{\circ}\text{C}$ is the only temperature at which both FeCl_2 and (Zn,Fe)S could be
309 observed abundantly in the coatings. At lower temperatures only traces of sulfide could be detected in
310 the coatings, whereas at 708 ± 5 $^{\circ}\text{C}$ only traces of FeCl_2 were detected. At even higher temperatures
311 (825 ± 5 , 1005 ± 5 $^{\circ}\text{C}$) chlorides are absent from the coatings.

312 **4. Discussion**

313 Both the “gas deposition experiments” and the “metal reaction experiments” result in the
314 formation of mineral assemblages containing sulfides and chlorides, and both experimental
315 approaches reproduce the fumarolic alteration products observed in the lunar Apollo 16 „Rusty Rock”
316 66095. In the gas deposition experiments FeS, FeCl_2 and ZnS occur over the temperature range of
317 $538\text{-}638\pm 5$ $^{\circ}\text{C}$. In the metal reaction experiment the most extensive reaction and formation of both
318 (Zn,Fe)S and FeCl_2 occurred at 580 ± 5 $^{\circ}\text{C}$, which is an almost identical temperature range as the gas
319 deposition experiment. The two experiments suggest that 580 ± 50 $^{\circ}\text{C}$ is the temperature condition
320 under which fumarolic alteration occurred on the Moon, as recorded in the „Rusty Rock” samples.

321 In our dry high temperature experiments we did not observe any oxyhydroxides and oxides
322 that have been reported in the Apollo „Rusty Rock” samples, such as akaganéite ($\beta\text{-FeO}(\text{OH},\text{Cl})$),
323 goethite ($\alpha\text{-FeO}(\text{OH})$) or hematite ($\alpha\text{-Fe}_2\text{O}_3$) (Shearer et al., 2014). We conducted our experiments
324 with water free, dried reagents, following the proposed H-poor nature of the C-O-S-Cl gas phase
325 (Norman et al., 1995; Shearer et al., 2012; Shearer et al., 2014). Our experiments have consistently
326 reproduced the dry alteration phases observed in the „Rusty Rock”. This suggests, that the
327 oxyhydroxides are a secondary alteration product of the primary FeCl_2 formed at high temperature.

328 The textural evidence from the Apollo 16 sample suggests that oxyhydration did not form upon
329 exposure to a terrestrial atmosphere, but that akaganéite did replace lawrencite, based on the Cl-
330 isotopes (Shearer et al., 2014). This suggests that the initial fumarolic alteration phase at 580 ± 50 °C
331 was followed by a secondary alteration phase at lower temperatures and with a gas at higher fH_2 and
332 fH_2O .

333 We performed our experiments in sealed and evacuated silica tubes with a 900 °C
334 temperature range. In such an experimental setup the direct control of gas fugacities (e.g. fO_2 and fS_2)
335 is not possible in the same way as in a conventional gas mixing furnace. Furthermore, the gas
336 fugacities may vary along the temperature gradient, as well as over time as phases are deposited from
337 the gas phase or gas species are bound to solids via chemisorption (King et al., 2018; Nekvasil et al.,
338 2019). In addition, gas-solid reaction experiments may be kinetically limited (Renggli and King,
339 2018), as they are in nature (King et al., 2018). However, the large temperature gradient, variations in
340 gas fugacities with temperature and time, as well as pressure increase with volatilization of elements
341 at high temperature, followed by a pressure decrease as phases deposit from the gas at lower
342 temperatures, are analogous to natural fumarolic processes (Henley and Seward, 2018). We argue that
343 our experimental approach adequately represents these natural systems (Renggli and Klemme, 2020).
344 Furthermore, some first order estimates on the gas composition can be made based on the phases
345 observed in the experiments and in the lunar „Rusty Rock”.

346 **4.1 Constraints on the gas phase composition**

347 As mentioned above, the starting material used in our experiments contained graphite powder
348 (Table 1) and it was placed in graphite crucibles. Graphite acts as a strong reducing agent and limits
349 the fO_2 at the source at 1240 °C, as any free oxygen will react with the excess graphite to form CO
350 gas. This is in analogy to the formation of CO-rich lunar volcanic gas that was argued to have formed
351 by the oxidation of graphite (Fogel and Rutherford, 1995; Nicholis and Rutherford, 2009). The CO-
352 bearing gas includes gaseous Zn and O due to the decomposition of ZnO and reaction with graphite.
353 A second decomposition process follows the equations $ZnO + MgCl_2 = ZnCl_{2(g)} + MgO$ or $ZnO +$
354 $MgCl_2 = Zn_{(g)} + Cl_{2(g)} + MgO$, but these do not directly impinge on the oxygen fugacity.

355 At lower temperatures gas compositions, or gas fugacities, are assessed based on the phase
356 assemblages observed in the experiments and the lunar „Rusty Rock”. First, we discuss the “gas
357 deposition experiments”. All chalcocite crystals deposited between 880-1140 °C show the growth of
358 Cu metal whiskers on the surface (Fig. 2a &b). Metal whiskers on sulfides are an indication of a
359 decrease in f_{S_2} after the formation of the sulfides in a low pressure environment (Wagner, 1952;
360 Nicolle and Rist, 1979). For example, iron whiskers were observed on sulfide grains in samples from
361 asteroid 25143 Itokawa, sampled by Hayabusa (Matsumoto et al., 2020). The observation of Cu metal
362 whiskers on the Cu_2S grains illustrates that the gas fugacities in our runs are not constant over time.
363 Initially, the Zn-Cu-Fe-C-O-S-Cl compounds in the source volatilize rapidly which results in
364 increasing gas pressure in the silica glass tube. As sulfides and chlorides deposit from the gas phase
365 along the temperature gradient the gas pressure decreases again. The sole species remaining
366 abundantly in the gas phase is CO, controlled by the reaction of excess graphite with any available
367 oxygen in the source at 1240 °C. We therefore assume that $\log f_{O_2}$ remains constant with time, but
368 $\log f_{S_2}$ decreases as the sulfides are deposited. The formation of the Cu metal whiskers suggests that
369 $\log f_{S_2}$ drops to the phase boundary of Cu_2S and Cu in the $\log f_{S_2}$ - $\log f_{O_2}$ space, as indicated by the
370 arrow in Figure 6a.

371 The occurrence of FeS and $FeCl_2$ together in both experimental approaches in the temperature
372 range 580 ± 50 °C, which we identified as the temperature condition forming the „Rusty Rock”
373 alteration on the Moon, allows further constraints of $\log f_{S_2}$ and $\log f_{Cl_2}$ in the experiment and for the
374 lunar „Rusty Rock”. The presence of both FeS and $FeCl_2$ (Fig. 2d for the gas deposition experiment
375 and Fig. 4i for the metal reaction experiment) constrains the two variables to the univariate line
376 indicated in Figure 6b. At 600 °C $\log f_{S_2}$ is in the range of -13.2 to -10.5 and $\log f_{Cl_2}$ is in the range of
377 -13.9 to -12.5 (Fig. 6b).

378 Finally, in the Fe “metal reaction experiments” the redox state, at least in the colder parts of
379 the tube, is further constrained by the Fe metal chips at 396 ± 5 , 496 ± 5 , 580 ± 5 , 708 ± 5 , 825 ± 5 and
380 1005 ± 5 °C. As we did not observe any oxidized iron in the experiments, we conclude that the $\log f_{O_2}$

381 remained below the iron-wüstite (IW) buffer at all temperatures and for the entire duration of the
382 experiment.

383 Recent calculations of a lunar volcanic gas phase revealed that main gas species are S₂, CO
384 and H₂ at 1200 °C, 10⁻⁶ bar and reducing conditions of IW-2 (Renggli et al., 2017). This model was
385 based on measurements of the volatiles H, S, Cl, F and C in partially degassed lunar pyroclastic glass
386 beads (Saal et al., 2008; Wetzel et al., 2015). In such a volcanic gas composition the metals primarily
387 deposit as sulfides with only minor abundances of elemental metal. Zink, Fe, Ni and Cu were
388 observed as sulfides in coatings on the pyroclastic glass beads and the only chloride that was observed
389 was NaCl (Butler and Meyer, 1976; Wasson et al., 1976; Clanton et al., 1978; Cirlin and Housley,
390 1979). Iron and Zn-chlorides, as observed in the Apollo 16 „Rusty Rock”, and in our experiments, are
391 not predicted as deposited solids in the thermodynamic model and were not observed in pyroclastic
392 glass bead coatings (Renggli et al., 2017). As a consequence, we suggest that the gas composition
393 forming the „Rusty Rock” alteration had a different composition than the volcanic gas driving
394 pyroclastic eruptions. Specifically, the log/Cl₂ must have been orders of magnitude higher in the
395 „Rusty Rock” alteration environment, compared to the pyroclastic gas, allowing the deposition of
396 metal chlorides from the gas phase and the reaction of Fe metal in the host rock to chloride.
397 Commonly used 50% condensation temperatures (Lodders, 2003) suggest deposition of Fe above
398 1300 °C (Day et al., 2019). However, our experimental results showed that FeCl₂ are deposited from a
399 gas phase at temperatures as low as 540 °C. This underlines the importance of experimental
400 exploration of a broader range of gas compositions from which metals deposit and condensate in
401 planetary environments. Finally, in our experiments, the relative abundances of Fe-, Zn-, and Cu-
402 phases were limited by the addition of these metals to the starting materials in equal molar
403 abundances (Table 1). These abundances do not represent those in the lunar samples, but were chosen
404 to allow a better comparison of the behavior of these metals in our experiments.

405 Note that the sulfide mineralization was not just observed in the Apollo 16 „Rusty Rock” but
406 sulfides have been observed in other Apollo 16 samples, including 67016 (Norman, 1981; Norman et
407 al., 1995; Shearer et al., 2012), as well as Apollo 11, 14 and 17 rocks (McKay et al., 1972; Ramdohr,

408 1972; Elardo et al., 2012). However, these rocks do not show chloride alteration and the predominant
409 sulfide phase is troilite (Shearer et al., 2012). In our experiment FeS was deposited from the gas phase
410 at 638 ± 5 - 698 ± 5 °C (Fig. 3). In addition to sulfide veins, likely deposited from a reducing S-rich gas,
411 troilite also occurs in metasomatic replacement textures of olivine to troilite and low-Ca pyroxene
412 (Colson, 1992; Norman et al., 1995; Shearer et al., 2012). In an ongoing study we will further
413 investigate the conditions under which these metasomatic replacement reactions occurred. At more
414 oxidizing conditions sulfates rapidly form when SO₂ reacts with basaltic glasses and minerals (King et
415 al., 2018; Renggli et al., 2019a). At reducing conditions relevant to the Moon and Mercury (Blewett et
416 al., 2013; Nittler et al., 2014) sulfides are predicted to form in a S-rich environment. At 700 °C and an
417 oxygen fugacity <IW additional sulfides may form including Na-, Ca- and Mg-sulfides (Renggli et al.,
418 2019b).

419 **5. Conclusions**

420 We conducted gas deposition and metal reaction experiments to simulate fumarolic alteration
421 in the Apollo 16 „Rusty Rock” 66095. The silica glass tube experiments are a useful tool to explore
422 metal transport processes and gas-solid reactions, such as sulfidation processes. Our experiments
423 indicate that the observed mineral assemblage of the rusty rock was formed at 580 ± 50 °C. In this
424 temperature range we observed the deposition of FeCl₂, ZnS and FeS in the gas deposition
425 experiment, and the formation of FeCl₂ and (Zn,Fe)S coatings on Fe metal grains reacted with a Zn-
426 C-O-S-Cl gas. The gas deposition experiments also showed that Cu₂S was deposited at higher
427 temperatures above 880 °C. Consequently, if Cu was carried in the lunar fumarolic gas, it must have
428 been deposited at higher temperatures and therefore likely at greater depths in the lunar crust
429 compared to the „Rusty Rock” alteration. This result supports the hypothesis that Cu was not
430 introduced into the „Rusty Rock” by a fumarolic gas, but was already present in the host rock, as
431 suggested by the normal lunar mare basalt $\delta^{65}\text{Cu}$ composition (Day et al., 2019). Our experiments do
432 not allow us to discriminate between the deposition of FeCl₂ and FeS from the fumarolic gas vs. the
433 in-situ reaction of metallic iron with a C-O-S-Cl gas. Both processes result in the formation of FeCl₂
434 and FeS in the temperature range of 580 ± 50 °C. The observed assemblage of FeCl₂ and FeS, and the

435 absence of oxidized iron, allowed us to constrain sulfur and chlorine fugacities in the gas phase at
436 reducing conditions below the IW buffer. At 600 °C $\log f_{S_2}$ is at -13.5 to -10.5 and $\log f_{Cl_2}$ is at -13.9
437 to -12.5.

438 **Acknowledgments**

439 Renggli is supported by a SNSF Early Postdoc.Mobility fellowship P2SKP2_181367. This
440 research was partially supported by DFG project 263649064 – SFB TRR-170, publication number
441 xxxx. Our thanks also go to M. Feldhaus, P. Weitkamp, L. Buxtrup, A. Hardes and S. Flunkert for
442 help and support in the laboratories at WWU Münster. No additional data were used in the preparation
443 of this manuscript. We thank Justin Filiberto for the editorial handling of this manuscript, and Gokce
444 Ustunisik, Malcolm Rutherford and Hanna Nekvasil for their helpful reviews that significantly
445 improved this manuscript.

446 **References**

- 447 Blewett D. T., Vaughan W. M., Xiao Z., Chabot N. L., Denevi B. W., Ernst C. M., Helbert J.,
448 D'Amore M., Maturilli A., Head J. W. and Solomon S. C. (2013) Mercury's hollows:
449 Constraints on formation and composition from analysis of geological setting and spectral
450 reflectance. *J. Geophys. Res. Planets* **118**, 1013–1032.
- 451 Butler P. and Meyer C. (1976) Sulfur prevails in coatings on glass droplets - Apollo 15 green and
452 brown glasses and Apollo 17 orange and black (devitrified) glasses. *Proc. Lunar Sci. Conf.* **7**,
453 1561–1581.
- 454 Chase M. W. (1998) *NIST-JANAF Thermochemical Tables*. 4th ed., Physical and Chemical Reference
455 Data.
- 456 Cirlin E. H. and Housley R. M. (1979) Scanning Auger Microprobe and atomic absorption studies of
457 lunar volcanic volatiles. In *Planetary Science Conference Proceedings*. pp. 341–354.
- 458 Clanton U. S., McKay D. S., Waits G. and Fuhrman R. (1978) Sublimate morphology on 74001 and
459 74002 orange and black glassy droplets. *Lunar Planet. Sci. Conf.* **9**, 1945–1957.
- 460 Colson R. O. (1992) Mineralization on the Moon?: Theoretical Considerations of Apollo 16 “Rusty
461 Rocks,” Sulfide Replacement in 67016, and Surface-Related Volatiles on Lunar Volcanic
462 Glass. *Proc. Lunar Planet. Sci.* **22**, 427–436.
- 463 Dalby K. N., Berger J. A., Brand H. E. A., Cairney J. M., Eder K., Eggins S. M., Herring A., Hervig
464 R. L., Krieder P. B., Mernagh T. P., Palm A. B., Renggli C. J., Troitzsch U., Yue L. and King
465 P. L. (2018) Analytical Techniques for Probing Small-Scale Layers that Preserve Information
466 on Gas–Solid Interactions. *Rev. Mineral. Geochem.* **84**, 103–175.

- 467 Day J. M. D., Moynier F. and Shearer C. K. (2017) Late-stage magmatic outgassing from a volatile-
468 depleted Moon. *Proc. Natl. Acad. Sci.*, 201708236.
- 469 Day J. M. D., Sossi P. A., Shearer C. K. and Moynier F. (2019) Volatile distributions in and on the
470 Moon revealed by Cu and Fe isotopes in the ‘Rusty Rock’ 66095. *Geochim. Cosmochim.*
471 *Acta*, S0016703719301218.
- 472 El Goresy A., Ramdohr P., Pavićević M., Medenbach O., Müller O. and Gentner W. (1973) Zinc,
473 lead, chlorine and FeOOH-bearing assemblages in the Apollo 16 sample 66095: Origin by
474 impact of a comet or a carbonaceous chondrite? *Earth Planet. Sci. Lett.* **18**, 411–419.
- 475 Elardo S. M., McCubbin F. M. and Shearer C. K. (2012) Chromite symplectites in Mg-suite troctolite
476 76535 as evidence for infiltration metasomatism of a lunar layered intrusion. *Geochim.*
477 *Cosmochim. Acta* **87**, 154–177.
- 478 Fogel R. A. and Rutherford M. J. (1995) Magmatic volatiles in primitive lunar glasses: I. FTIR and
479 EPMA analyses of Apollo 15 green and yellow glasses and revision of the volatile-assisted
480 fire-fountain theory. *Geochim. Cosmochim. Acta* **59**, 201–215.
- 481 Gargano A., Sharp Z., Shearer C., Simon J. I., Halliday A. and Buckley W. (2020) The Cl isotope
482 composition and halogen contents of Apollo-return samples. *Proc. Natl. Acad. Sci.*,
483 202014503.
- 484 Haskin L. A. and Warren P. (1991) Lunar Chemistry. In *Lunar source book* (eds. G. H. Heiken, D. T.
485 Vaniman, and B. V. French). Cambridge University Press, New York. pp. 357–474.
- 486 Henley R. W. and Seward T. M. (2018) Gas–Solid Reactions in Arc Volcanoes: Ancient and Modern.
487 *Rev. Mineral. Geochem.* **84**, 309–349.
- 488 Hunter R. H. and Taylor L. A. (1981a) Rust and schreibersite in Apollo 16 highland rocks:
489 Manifestations of volatile-element mobility. In *Lunar and Planetary Science Conference*
490 *Proceedings* 253-259.
- 491 Hunter R. H. and Taylor L. A. (1981b) Rusty Rock 66095: A paradigm for volatile-element mobility
492 in highland rocks. In *Lunar and Planetary Science Conference Proceedings*
- 493 Jean M. M., Bonder B., Farley C. and Taylor L. A. (2016) “Rusty Rocks” from the Moon: Volatile-
494 Element Contributions from Meteorites. In *Lunar and Planetary Science Conference*. p. 2498.
495 Available at: <http://adsabs.harvard.edu/abs/2016LPI...47.2498J> [Accessed August 7, 2019].
- 496 Kerridge J. F., Kaplan I. R., Petrowski C. and Chang S. (1975) Light element geochemistry of the
497 Apollo 16 site. *Geochim. Cosmochim. Acta* **39**, 137–162.
- 498 King P. L., Wheeler V. M., Renggli C. J., Palm A. B., Wilson S. A., Harrison A. L., Morgan B.,
499 Nekvasil H., Troitzsch U., Mernagh T., Yue L., Bayon A., DiFrancesco N. J., Baile R.,
500 Kreider P. and Lipi W. (2018) Gas–Solid Reactions: Theory, Experiments and Case Studies
501 Relevant to Earth and Planetary Processes. *Rev. Mineral. Geochem.* **84**, 1–56.
- 502 Krähenbühl U., Ganapathy R., Morgan J. A. and Anders E. (1973) Volatile elements in Apollo 16
503 samples: implications for highland volcanism and accretion history of the moon. In
504 *Proceedings of the 4th Lunar Science Conference*. Pergamon Press, New York. pp. 1325–
505 1348.
- 506 Lodders K. (2003) Solar System Abundances and Condensation Temperatures of the Elements.
507 *Astrophys. J.* **591**, 1220.

- 508 Matsumoto T., Harries D., Langenhorst F., Miyake A. and Noguchi T. (2020) Iron whiskers on
509 asteroid Itokawa indicate sulfide destruction by space weathering. *Nat. Commun.* **11**, 1–8.
- 510 McCubbin F. M., Kaaden K. E. V., Tartèse R., Klima R. L., Liu Y., Mortimer J., Barnes J. J., Shearer
511 C. K., Treiman A. H., Lawrence D. J., Elardo S. M., Hurley D. M., Boyce J. W. and Anand
512 M. (2015) Magmatic volatiles (H, C, N, F, S, Cl) in the lunar mantle, crust, and regolith:
513 Abundances, distributions, processes, and reservoirs. *Am. Mineral.* **100**, 1668–1707.
- 514 McKay D. S., Clanton U. S., Morrison D. A. and Ladle, G.H. (1972) Vapor phase crystallization in
515 Apollo 14 breccia. In *Proceedings of the Third Lunar Science Conference* pp. 739–752.
- 516 Meyer C. (2009) 66095 “Rusty Rock.” *Lunar Sample Compend.*, 22.
- 517 Nekvasil H., DiFrancesco N. J., Rogers A. D., Coraor A. E. and King P. L. (2019) Vapor-Deposited
518 Minerals Contributed to the Martian Surface During Magmatic Degassing. *J. Geophys. Res.*
519 *Planets* **124**, 1592–1617.
- 520 Nicholis M. G. and Rutherford M. J. (2009) Graphite oxidation in the Apollo 17 orange glass magma:
521 Implications for the generation of a lunar volcanic gas phase. *Geochim. Cosmochim. Acta* **73**,
522 5905–5917.
- 523 Nicolle R. and Rist A. (1979) The mechanism of whisker growth in the reduction of wüstite. *Metall.*
524 *Trans. B* **10**, 429–438.
- 525 Nittler L. R., Weider S. Z., Starr R. D., Chabot N., Denevi B. W., Ernst C. M., Goudge T. A., Head J.
526 W., Helbert J., Klima R. L., McCoy T. J. and Solomon S. C. (2014) Sulfur-Depleted
527 Composition of Mercury’s Largest Pyroclastic Deposit: Implications for Explosive Volcanism
528 and Surface Reflectance on the Innermost Planet. *Lunar Planet. Sci. Conf.* **45**, 1391.
- 529 Norman M. D. (1981) Petrology of suevitic lunar breccia 67016. In *Proc. Lunar Planet. Sci.* pp. 235–
530 252.
- 531 Norman M. D., Keil K., Griffin W. L. and Ryan C. G. (1995) Fragments of ancient lunar crust:
532 Petrology and geochemistry of ferroan noritic anorthosites from the Descartes region of the
533 Moon. *Geochim. Cosmochim. Acta* **59**, 831–847.
- 534 Norris C. A. and Wood B. J. (2017) Earth’s volatile contents established by melting and vaporization.
535 *Nature* **549**, 507–510.
- 536 Papike J. J., Taylor L. A. and Simon S. (1991) Lunar minerals. In *Lunar source book* (eds. G. H.
537 Heiken, D. T. Vaniman, and B. V. French). Cambridge University Press, New York. pp. 357–
538 474.
- 539 Ramdohr P. (1972) Lunar pentlandite and sulfidization reactions in microbreccia 14315, 9. *Earth*
540 *Planet. Sci. Lett.* **15**, 113–115.
- 541 Renggli C. J. and King P. L. (2018) SO₂ Gas Reactions with Silicate Glasses. *Rev. Mineral.*
542 *Geochem.* **84**, 229–255.
- 543 Renggli C. J., King P. L., Henley R. W. and Norman M. D. (2017) Volcanic gas composition, metal
544 dispersion and deposition during explosive volcanic eruptions on the Moon. *Geochim.*
545 *Cosmochim. Acta* **206**, 296–311.
- 546 Renggli C. J. and Klemme S. (2020) Experimental constraints on metal transport in fumarolic gases.
547 *J. Volcanol. Geotherm. Res.* **400**, 106929.

- 548 Renggli, King P. L., Henley R. W., Guagliardo P., McMorro L., Middleton J. P. and Turner M.
549 (2019a) An experimental study of SO₂ reactions with silicate glasses and supercooled melts
550 in the system anorthite–diopside–albite at high temperature. *Contrib. Mineral. Petrol.* **174**, 3.
- 551 Renggli, Palm A. B., King P. L. and Guagliardo P. (2019b) Implications of Reactions Between SO₂
552 and Basaltic Glasses for the Mineralogy of Planetary Crusts. *J. Geophys. Res. Planets* **124**,
553 2563–2582.
- 554 Roine A. (2015) *Outotec HSC Chemistry 8.1.*, Outotec Research Center, Finland.
- 555 Saal A. E., Hauri E. H., Cascio M. L., Van Orman J. A., Rutherford M. C. and Cooper R. F. (2008)
556 Volatile content of lunar volcanic glasses and the presence of water in the Moon’s interior.
557 *Nature* **454**, 192–195.
- 558 Sharp Z. D., Shearer C. K., McKeegan K. D., Barnes J. D. and Wang Y. Q. (2010) The Chlorine
559 Isotope Composition of the Moon and Implications for an Anhydrous Mantle. *Science* **329**,
560 1050–1053.
- 561 Shearer C. K., Burger P. V., Guan Y., Papike J. J., Sutton S. R. and Atudorei N.-V. (2012) Origin of
562 sulfide replacement textures in lunar breccias. Implications for vapor element transport in the
563 lunar crust. *Geochim. Cosmochim. Acta* **83**, 138–158.
- 564 Shearer C. K., Sharp Z. D., Burger P. V., McCubbin F. M., Provencio P. P., Brearley A. J. and Steele
565 A. (2014) Chlorine distribution and its isotopic composition in “rusty rock” 66095.
566 Implications for volatile element enrichments of “rusty rock” and lunar soils, origin of “rusty”
567 alteration, and volatile element behavior on the Moon. *Geochim. Cosmochim. Acta* **139**, 411–
568 433.
- 569 Sossi P. A. and Fegley B. (2018) Thermodynamics of Element Volatility and its Application to
570 Planetary Processes. *Rev. Mineral. Geochem.* **84**, 393–459.
- 571 Sossi P. A., Klemme S., O’Neill H. St. C., Berndt J. and Moynier F. (2019) Evaporation of
572 moderately volatile elements from silicate melts: experiments and theory. *Geochim.*
573 *Cosmochim. Acta* **260**, 204–231.
- 574 Taylor L. A., Mao H. K. and Bell P. M. (1974) Identification of the Hydrated Iron Oxide Mineral
575 Akaganéite in Apollo 16 Lunar Rocks. *Geology* **2**, 429–432.
- 576 Taylor L. A., Mao H. K. and Bell P. M. (1973) “Rust” in the Apollo 16 rocks. In *Proc. 4th Lunar Sci.*
577 *Conf.* pp. 829–839.
- 578 Ustunisik G., Nekvasil H., Lindsley D. H. and McCubbin F. M. (2015) Degassing pathways of Cl-, F-
579 , H-, and S-bearing magmas near the lunar surface: Implications for the composition and Cl
580 isotopic values of lunar apatite. *Am. Mineral.* **100**, 1717–1727.
- 581 Wagner C. (1952) Mechanism of the Reduction of Oxides and Sulphides to Metals. *JOM* **4**, 214–216.
- 582 Wang Y., Guan Y., Hsu W. and Eiler J. M. (2012) Water Content, Chlorine and Hydrogen Isotope
583 Compositions of Lunar Apatite. *Meteorit. Planet. Sci. Suppl.* **75**, 5170.
- 584 Wasson J. T., Boynton W. V., Kallemeyn G. W., Sundberg L. L. and Wai C. M. (1976) Volatile
585 compounds released during lunar lava fountaining. *Proc. Lunar Sci. Conf.* **7**, 1583–1595.
- 586 Wetzel D. T., Hauri E. H., Saal A. E. and Rutherford M. J. (2015) Carbon content and degassing
587 history of the lunar volcanic glasses. *Nat. Geosci.* **8**, 755–758.

588

589

590 **Tables**

591 *Table 1: Composition of the experimental charges of the gas deposition and metal reaction*
 592 *experiments. The table shows nominal molar concentrations of the reagent mixtures and weighed-in*
 593 *values.*

	Gas deposition experiment		Metal reaction experiment	
	Molar abundances	Weight g	Molar abundances	Weight g
ZnO	1	0.0068(1)	1	0.0158(1)
FeS	1	0.0073(1)	-	-
CuS	1	0.0080(1)	-	-
MgCl ₂	3	0.0239(1)	1	0.0185(1)
S	-	-	1	0.0062(1)
C	4	0.0040(1)	4	0.0094(1)
Total		0.05		0.05

594

595 *Table 2: Experimental conditions and positions of Fe metal chips along the silica tube in the*
 596 *metal reaction experiment. Temperatures were measured with a type B thermocouple in the vertical*
 597 *tube furnace in 1 cm steps prior to the experiments.*

	Distance from top of tube	Temperature
	cm	°C
a	7	396±5
b	11	496±5
c	13	580±5
d	15	708±5
e	17	825±5
f	21	1005±5
Volatile source	31	1240±5
Tube length		28 cm
Duration		24h

598

599

600

601

602

603

604 *Table 3: EDS analysis of the observed phases in the “gas deposition experiment” given in*
 605 *atomic %. Standard deviations of the analyses are given in brackets. Backscattered electron images of*
 606 *the analyzed phases are shown in Fig. 2.*

Temperature °C	Phase	S atomic %	Cl atomic %	Fe atomic %	Cu atomic %	Zn atomic %
300-538	ZnCl ₂	n.d.	59.0(1.7)	0.9(0.7)	n.d.	39.9(1.9)
498-538	Zn-Cl-S	22.8(1.3)	30.8(6.3)	0.5(0.2)	n.d.	45.9(7.3)
538-587	ZnS	43.0(2.1)	6.5(0.7)	3.7(0.4)	0.8(0.1)	46.0(2.1)
538-698	FeCl ₂	1.9(2.2)	61.1(3.5)	36.6(1.3)	n.d.	0.3(0.1)
638-698	FeS	44.4(1.9)	4.5(2.2)	50.0(2.7)	0.9(0.3)	n.d.
698-830	Cu-Fe-Cl-S	31.5(3.0)	20.5(3.2)	16.2(3.9)	31.6(3.5)	n.d.
878-1140	Cu ₂ S	35.0(2.5)	2.8(1.0)	6.4(0.8)	55.7(2.0)	n.d.
878-1140	Cu (whiskers)	5.1(2.7)	2.0(1.3)	2.4(1.4)	90.5(3.7)	n.d.

607 n.d. = not detected, i.e., below the detection limit

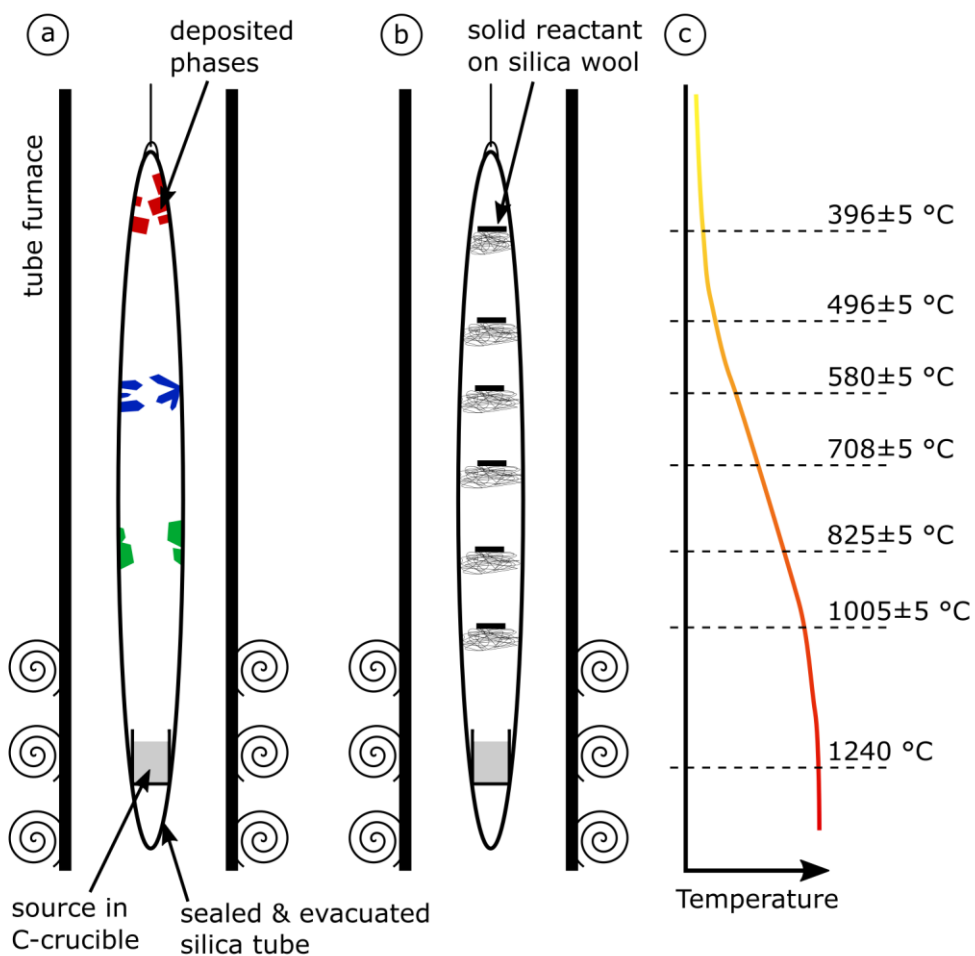
608

609 *Table 4: EDS analysis of the observed mineral phases in the “metal reaction experiment”*
 610 *given in atomic %. Standard deviations of the analyses are given in brackets. Backscattered electron*
 611 *images of the analyzed phases are shown in Figs. 3 and 4.*

Temperature °C	Phase	S atomic %	Cl atomic %	Fe atomic %	Zn atomic %
396	FeCl ₂	n.d.	65.3(2.2)	34.1(2.1)	n.d.
496	FeCl ₂	3.4(2.2)	59.9(6.4)	19.8(3.9)	16.9(1.6)
580	FeCl ₂	0.9(0.6)	61.1(3.8)	28.4(5.2)	9.6(1.9)
580	(Zn,Fe)S	49.5(0.3)	4.4(1.1)	2.7(0.2)	43.4(1.0)
708	FeCl ₂	1.2(0.7)	62.8(13.3)	28.4(15.7)	7.8(2.6)
708	(Zn,Fe)S	50.3(0.8)	n.d.	22.6(3.2)	26.9(3.2)
825	(Zn,Fe)S	50.7(0.2)	n.d.	18.3(1.4)	31.0(1.2)
825	(Fe,Zn)S	50.2(0.3)	n.d.	28.3(0.5)	21.5(0.3)
825	FeS	50.8(0.5)	n.d.	48.7(0.6)	0.4(0.1)
1005	(Zn,Fe)S	50.4(0.3)	n.d.	14.7(0.9)	34.8(0.6)
1005	(Fe,Zn)S	50.1(0.2)	n.d.	22.1(0.8)	27.8(1.0)

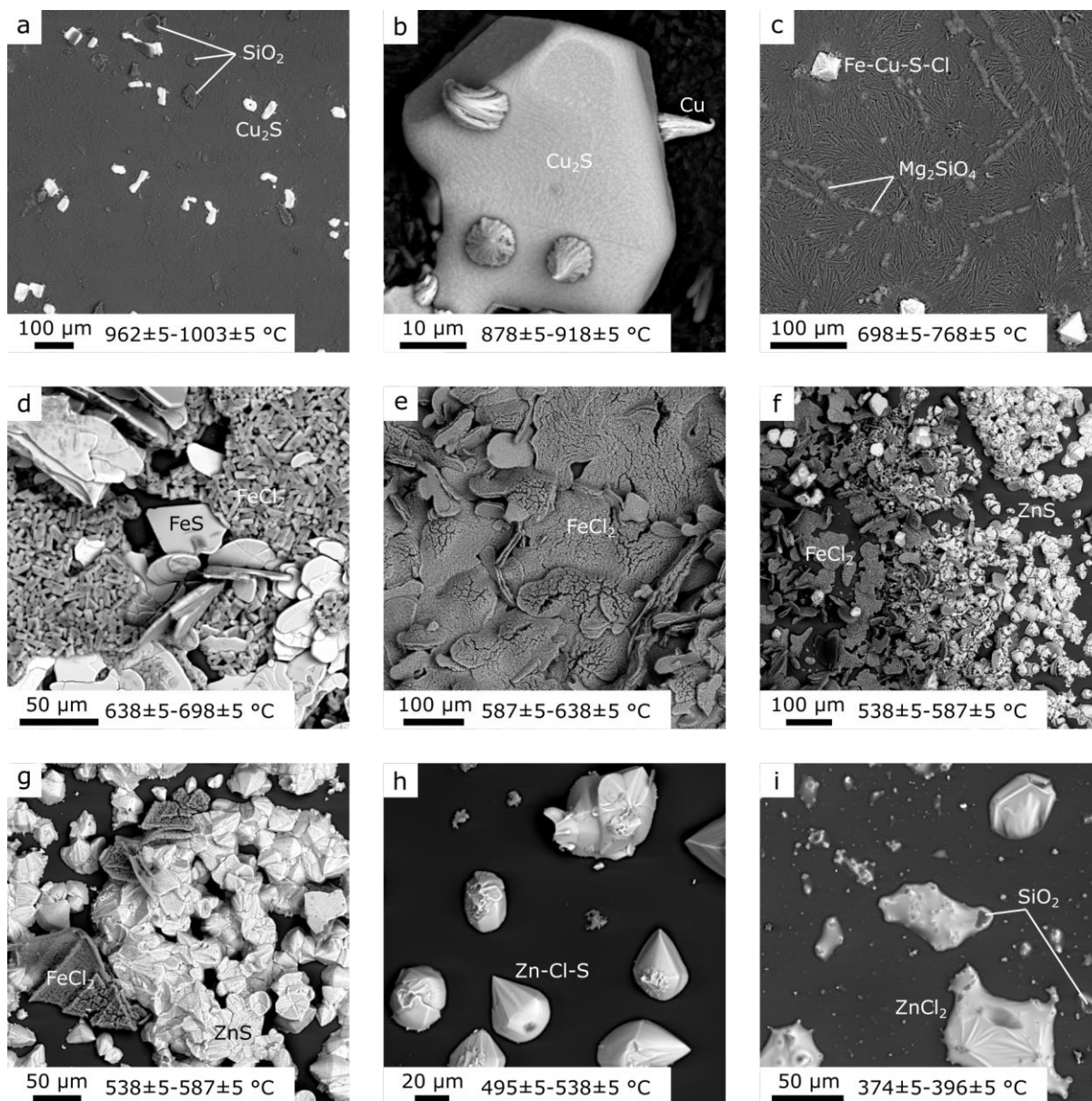
612 n.d. = not detected, i.e., below the detection limit

613



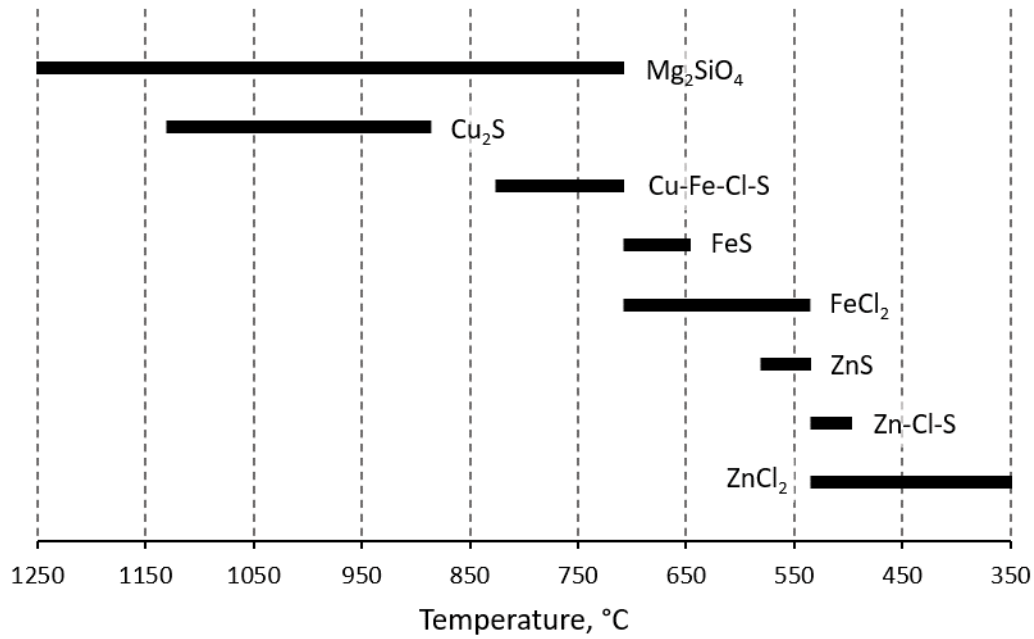
615

616 *Figure 1: Illustration of the experimental setup in a vertical tube furnace. a) Gas deposition*
 617 *experiment. The source in the hot zone of the furnace volatilizes and different phases are deposited*
 618 *along the temperature gradient within the silica glass tube.; b) Metal reaction experiment. The Fe*
 619 *metal chips were placed on SiO₂ glass wool spacers at 396±5, 496±5, 580±5, 708±5, 825±5 and*
 620 *1005±5 °C; c) schematic of the furnace temperature gradient with temperatures at which the Fe metal*
 621 *chips were placed within the tube.*



622

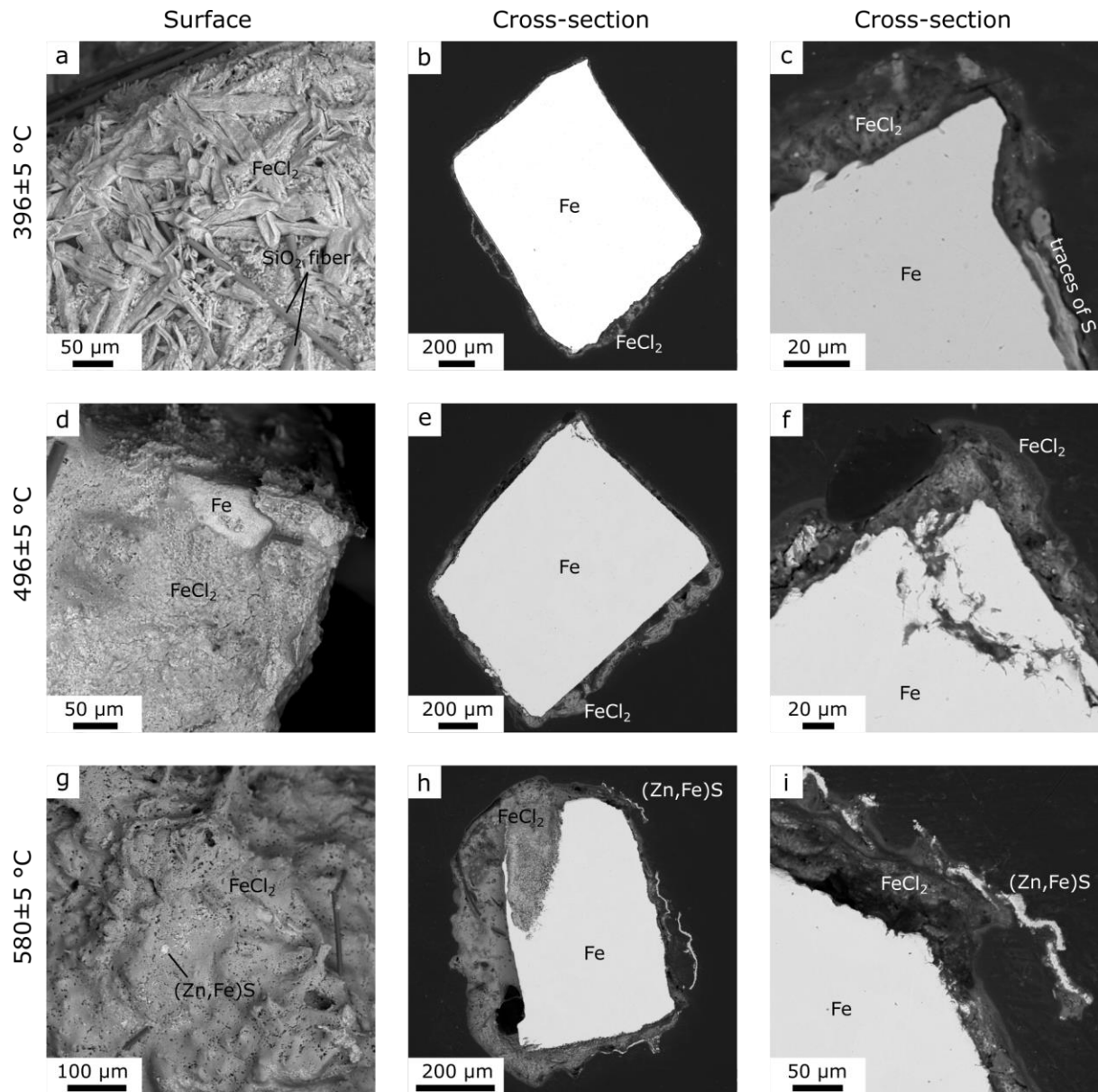
623 *Figure 2: Backscattered electron images of phases deposited on the inner silica tube wall (“gas*
 624 *deposition experiment”). a) Cu_2S grains and SiO_2 glass dust which was formed during opening of the*
 625 *tube, $962\pm 5\text{-}1003\pm 5$ °C; b) Cu_2S grain with Cu metal whiskers, $878\pm 5\text{-}918\pm 5$ °C; c) Unidentified Fe-*
 626 *Cu-S-Cl phase and Mg_2SiO_4 , the reaction product of MgO with the silica glass tube wall, $698\pm 5\text{-}$*
 627 *768 ± 5 °C; d) FeS and FeCl_2 , $638\pm 5\text{-}698\pm 5$ °C; e) FeCl_2 , $587\pm 5\text{-}638\pm 5$ °C; f) FeCl_2 and ZnS, $538\pm 5\text{-}$*
 628 *587 ± 5 °C; g) FeCl_2 and ZnS, $538\pm 5\text{-}587\pm 5$ °C; h) Unidentified Zn-Cl-S phase, $495\pm 5\text{-}538\pm 5$ °C; i)*
 629 *Liquidized and hydrated ZnCl_2 due to its deliquescence, SiO_2 glass shards, $374\pm 5\text{-}396\pm 5$ °C.*



630

631 *Figure 3: Distribution of phases deposited along the temperature gradient in the silica tube*
 632 *summarizing the observations shown in Fig. 2 from the gas deposition experiment. The solid bars*
 633 *show the temperature ranges over which the respective phases were observed in the silica glass tube*
 634 *by investigation of the inner tube wall with back-scattered electron microscopy and EDS analysis.*
 635 *„Rusty Rock” phases are observed over the temperature range 538 ± 5 - 638 ± 5 °C.*

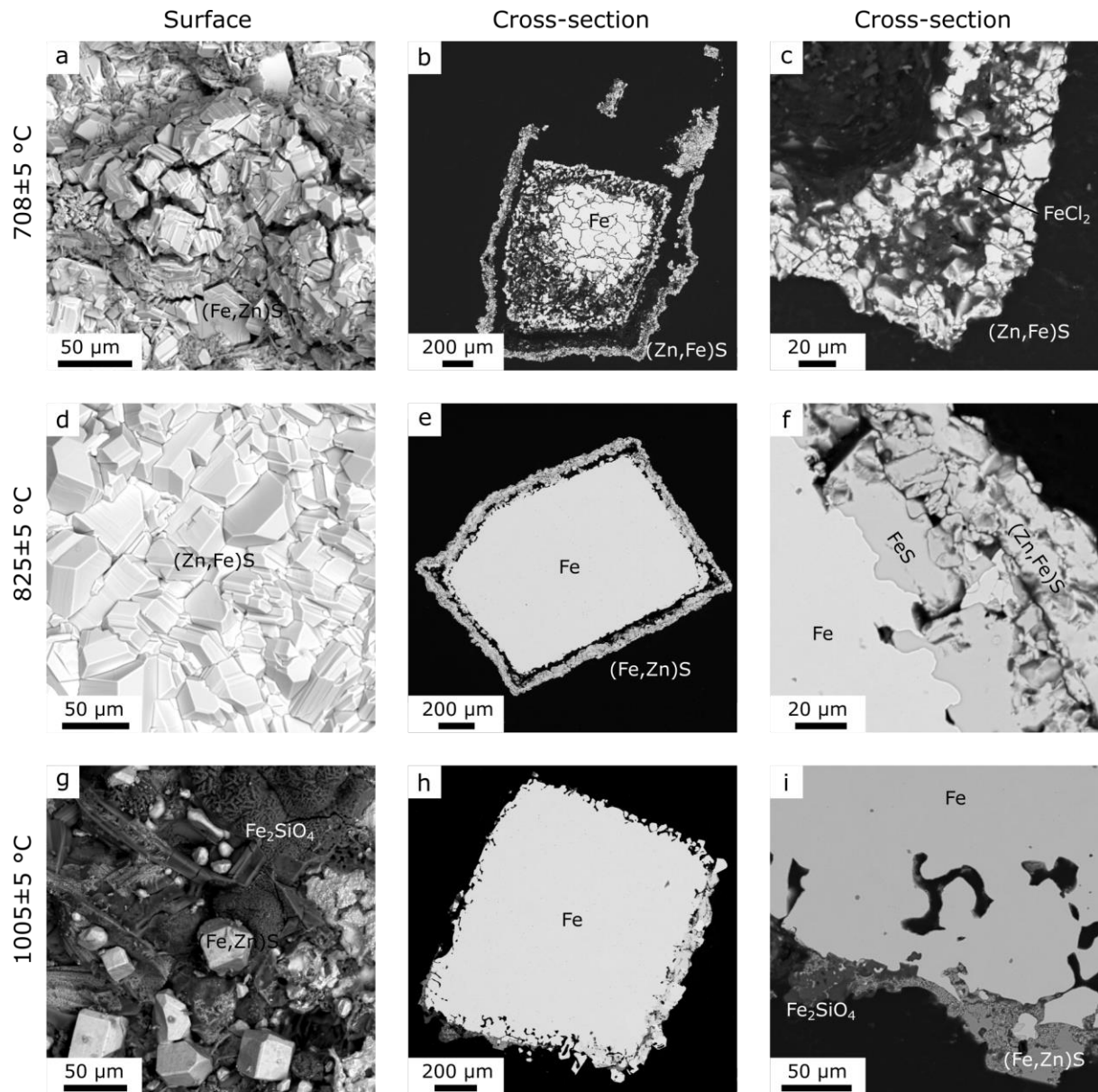
636



637

638 *Figure 4: Backscattered electron images of the Fe metal reaction experiment. Images a, d and c show*
 639 *the surfaces of the coatings and images b, c, e, f, h and I show cross-sections of the samples. The rows*
 640 *indicate the temperatures, 396±5 °C (a-c), 496±5 °C (d-f) and 580±5 °C (g-h).*

641

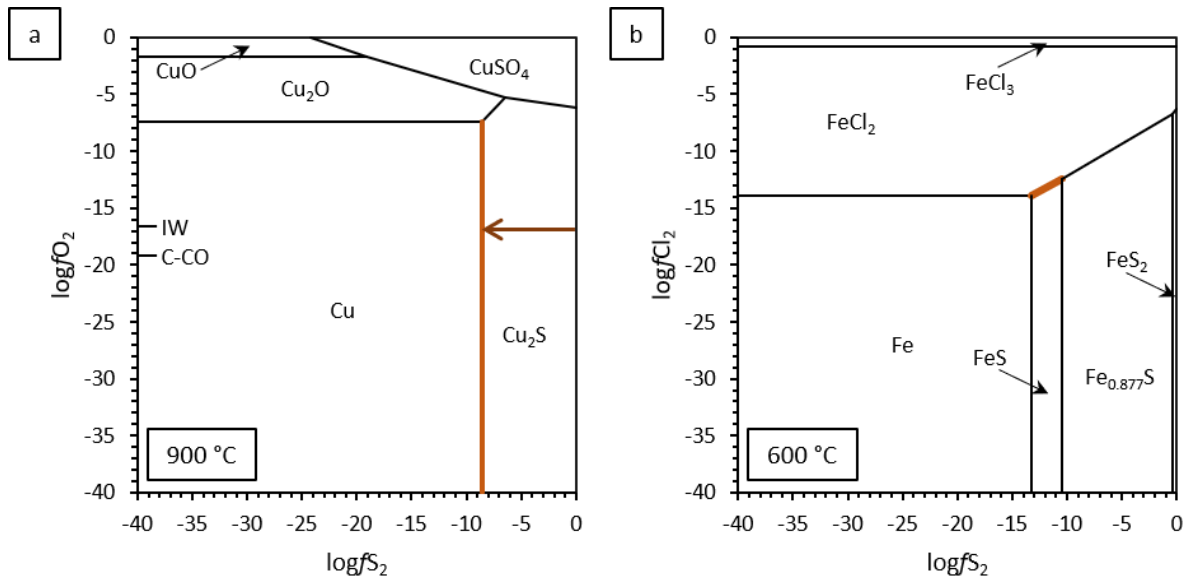


642

643 *Figure 5: Backscattered electron images of the Fe metal reaction experiment. Images a, d and c show*
 644 *the surfaces of the coatings and images b, c, e, f, h and I show cross-sections of the samples. The rows*
 645 *indicate the temperatures, 708±5 °C (a-c), 825±5 °C (d-f) and 1005±5 °C (g-h).*

646

647



648

649 *Figure 6: a) Phase stability diagram of the system Cu-S-O as a function of $\log f_{S_2}$ and $\log f_{O_2}$*
 650 *at 900 °C, 1 bar. The univariate line in brown shows the condition for coexistence of Cu and Cu₂S as*
 651 *observed in the metal transport experiment and the formation of Cu whiskers on the Cu₂S crystal. The*
 652 *brown arrow indicates a decrease in $\log f_{S_2}$ with experimental duration resulting in the growth of Cu*
 653 *whiskers. b) Phase stability diagram of the system Fe-S-Cl as a function of $\log f_{S_2}$ and $\log f_{Cl_2}$ at 600*
 654 *°C, 1 bar. The univariate line shows the co-stability of FeCl₂ and FeS as observed in the metal*
 655 *transport experiment at 638±5-698±5 °C (Fig. 2d) and the Fe metal-gas reaction experiment at*
 656 *580±5 °C (Fig. 4g-i). Calculations were made with the program HSC9 by Outotec, largely based on*
 657 *data from the NIST-JANAF thermochemical data base (Chase, 1998; Roine, 2015).*